# Evaluation of Automatic Microstructural Analysis of Energy Dispersive Spectroscopy (EDS) Maps via a Python-Based Data Processing Framework

ECS Transactions, 104 (8) 137-153 (2021)
10.1149/10408.0137ecst ©The Electrochemical Society

# Evaluation of Automatic Microstructural Analysis of Energy Dispersive Spectroscopy (EDS) Maps via a Python-Based Data Processing Framework

Mariah Batool[a], Richard Andres Ortiz Godoy[a,b], Martin Birnbach[b], Dario R. Dekel[c], Jasna Jankovic[a,b]

[a] Institute of Materials Science, University of Connecticut, 97 North Eagleville Road, Unit 3136, Storrs, CT 06269-3136

[b] Department of Materials Science & Engineering, University of Connecticut, 97 North Eagleville Road, Unit 3136, Storrs, CT 06269-3136

[c] The Wolfson Department of Chemical Engineering, and The Nancy & Stephen Grand Technion Energy Program (GTEP); Technion – Israel Institute of Technology, Haifa 3200003, Israel

## Abstract

Computer-aided data acquisition, analysis and interpretation have been employed in various research areas generating useful information. Among these, image processing is most often implemented for post-processing of material characterization data. However, to tackle ambiguity of multi-component materials analysis, spectral data analysis can be used instead. The current study introduces a unique Python-based data processing method for in-depth analysis of energy dispersive spectroscopy (EDS) elemental maps to analyze agglomerate size distribution, average area of each component and their overlap. The framework developed in this study is applied to examine interaction of Cerium (Ce) and Palladium (Pd) particles in membrane electrode assembly (MEA) of Anion-Exchange Membrane Fuel Cell (AEMFC) and investigate if this approach can be utilized to predict the fuel cell's electrochemical behavior. The study concludes that the developed framework is a promising method for automatic data extraction and can be beneficial for use in a variety of clean energy applications.

## Introduction

With the progression of materials from being discovered coincidentally to being designed and optimized strategically, there has been an imminent need to analyze and model materials for specific applications. This process can nowadays be facilitated by the power of microscopy and image processing (1). Image processing has found a plethora of applications in the field of materials science ranging from detailed morphological and structural analysis of materials to the study of their degradation and failure, including fuel cells (2–7). Image processing is most widely implemented to extract valuable information from a larger set of materials characterization data to better understand and predict material features, properties, and behaviors at multiple scales. To ensure accuracy of results obtained from image processing, it is vital for it to have a systematic recognition of volumetric data and the ability to process it swiftly, for an efficient analysis.

Unfortunately, image processing also comes with complications and challenges since microstructural images have a series of inherent properties that can cause analysis to be difficult for manual and automated techniques. Microscopic images are influenced by noise which is the inclusion of random and false signals due to external conditions produced by sensors, detectors, amplifiers etc., (8,9), and can make features like grain boundaries or materials interfaces difficult to perceive or can create the appearance of features that are not real. Consequently, it is appropriate to state that manual image processing is subjected to human error, experience and bias due to varying opinions on what constitutes a grain, grain boundary, defect, etc. within a microstructure. As a result, ensuing measurements are objective and statistically representative requires repetition of the measurements, which becomes a burdensome and time-consuming task. Manual methods are therefore very slow and laborious (10). With automation, microstructural analysis and measurements are conducted within seconds, can be repeated without any inter-operator variation, and human error is reduced. One of the most difficult tasks of automated image processing is guaranteeing that the software is representing the material features accurately. However, although computer-based automated image processing has its challenges, it is far more superior and has unarguably overshadowed manual image processing techniques in the recent decades.

The main process involves digitization of the image (11,12) which can be graphically represented by Figure 1.

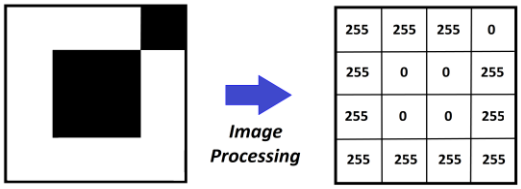


Figure 1: A graphical representation of how image processing works.

Such favorable characteristics of image processing led researchers to realize its potential for providing valuable microstructural information in the process of improving performance and efficiency of clean energy systems (13–15). Particularly, inspecting individual and collective characteristics of microstructural features of materials constituting a fuel cell such as electrodes, catalysts and electrolyte membranes can help predict electrochemical behavior down to nanometric scale (16). Beside composition, fuel cell performance and durability are known to depend on the electrode microstructure and component distribution. Therefore, to facilitate the development of efficient fuel cells and establish statistically relevant correlations between the microstructure and performance, automated image processing is required. Typically, the automated image processing for fuel cells involves particle or pore size distribution using Transmission Electron Microscopy (TEM) or Scanning Electron Microscopy (SEM), without taking into account elemental composition (17,18). However, using greyscale TEM and SEM images often makes it challenging to differentiate between various components in the material. Utilization of Scanning Transmission Electron Microscopy with Energy Dispersive Spectroscopy (STEM-EDS) provides elemental maps with spatial component distribution, enabling this differentiation and offering a whole range of new possibilities for automated sample analysis.

Several data processing approaches using EDS data, mainly in conjunction with SEM have been developed and reported for a wide range of applications such as automatic particle size analysis of nano-materials, mineral constituents in rocks, inclusions in metals, contaminants in pharmaceutical products, air or water particulates, gun-shot residue in forensic science, pathological tissue in biomedical research, automated identification of different phases and calculation of area, perimeter or compactness in a sample (19–26). Combined with machine and deep learning algorithms, SEM-EDS data have been used to automatically investigate the microstructural features, morphology, orientation and symmetry in samples and count, aspect ratio and dimensions of the features in the materials. However, apparently no such automated approach has been adopted and documented for anion exchange membrane fuel cells (AEMFCs) related research yet, especially not when using STEM-EDS.

In this study, a python-based data processing interface was developed and subsequently utilized to investigate STEM-EDS maps for Palladium (Pd)-based electrodes of AEMFCs. Pd based catalysts are known low-cost alternatives to expensive Platinum (Pt) catalysts used in lower operating temperature range fuel cells such as AEMFCs. However, this catalyst suffers from reduced hydrogen oxidation reaction (HOR) kinetics (27). It is reported that this problem could be potentially avoided by combining Pd with Cerium oxide ($CeO_x$) and ensuring sufficient Pd-$CeO_x$ interaction for increase in catalytic activity (28,29). In this work, we report testing of an in-house developed python-based code (30) to process Pd and Ce EDS maps for AEMFC catalyst layers, and determine Pd and Ce particle/agglomerate size distribution, as well as overlap area between Pd and Ce particles. The python interface uses microscopy and EDS elemental maps data of Pd-$CeO_x$ based catalyst to produce visual and numerical results with potential to predict the electrochemical performance and durability of the AEMFCs.

## Methodology

The script for the data processing framework developed in this study was written in Python programming language. The idea was built around the fact that materials characterization data about Pd-$CeO_x$ based catalyst, although can be a source of vast amount of information, it requires a rigorous analysis procedure to get “concealed” or underlying information not visible to the naked eye such as percentage of area where Pd and $CeO_x$ overlap (contact area, which is expected to benefit the HOR activity). Thus, three different catalyst samples, i.e., n $CeO_x$-Pd/C with varying compositions (where n denotes bulk atomic fraction of Ce/Pd) 0.24 CeOx-Pd/C, 0.38 CeOx-Pd/C and 0.59 CeOx-Pd/C labelled as DD08, DD09 and DD16, respectively were taken into consideration and three different maps of each sample were analyzed using the data processing interface. A graphical overview of the whole process is shown in Figure 2 and discussed below. A detailed description of the samples, their fabrication and testing are described in a study by Singh. et al (31).

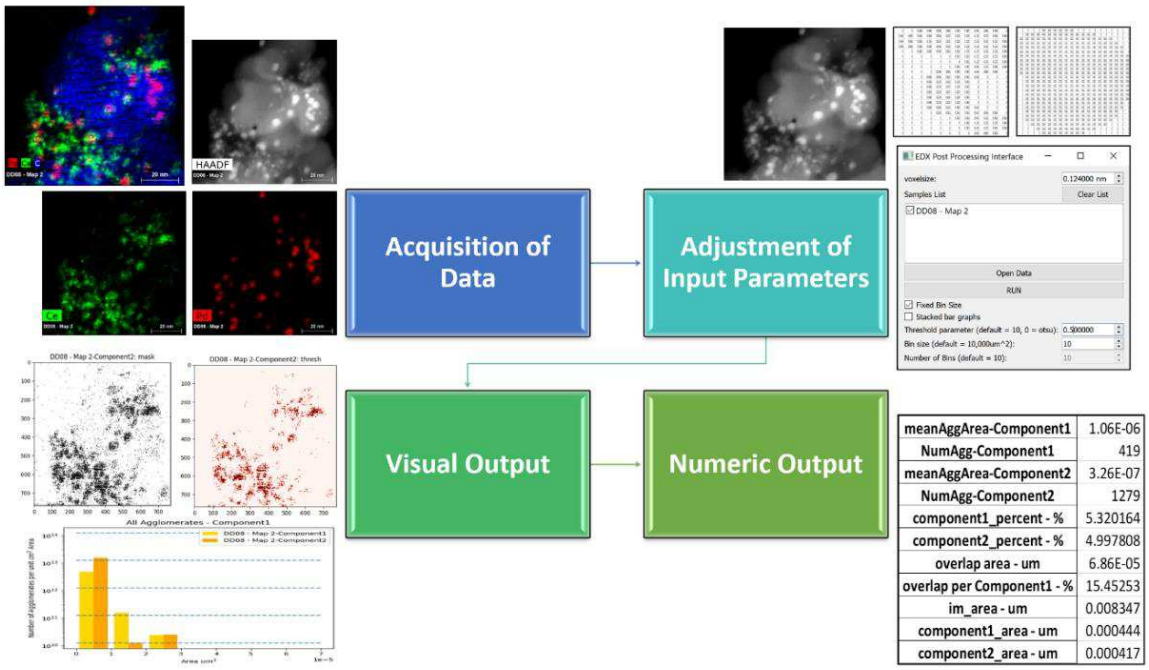


Figure 2: A graphical step-by-step overview of the data processing methodology

Acquisition and Processing of Raw Data

STEM-EDS mapping was used to take elemental maps of the MEA electrode cross-section. Images were obtained at a constant magnification of 910,000X using high-angle annular dark field (HAADF) imaging technique. This technique was combined with the EDS to get elemental maps. The type of raw maps that are obtained are shown in Figure 3. The raw maps were processed using the software Esprit (Version 1.9) to remove background and deconvolute the spectral peaks. The processed individual elemental maps of EDS X-ray net intensities of Ce and Pd were obtained and saved as text file in ASCII format. The software allocates a specific numeric value in the text file according to the X-ray net intensity data for each pixel of the map. However, the processing of the elemental maps can be performed using different binning (resolutions): e.g., with the resolution 1, each pixel is separately processed, and its processed value is assigned to the same pixel; with the resolution 0.5 (1/2), four pixels are averaged; with the resolution 0.125 (1/8), sixteen pixels are averaged; etc. Consequently, resulting net count values of same pixels (e.g., ascribed to a particle) in text files of the same map at different resolutions are very different. The net count values are smaller for lower resolution maps as compared to higher resolution maps. An example of different net count values at different map resolutions is shown in Figure 4. The name of all the text files for Pd were labelled as _component1.txt and all the text files for Ce were labelled as _component2.txt and saved in separate folders with each sample's name and map number. Furthermore, the STEM image for each map taken with HAADF imaging was saved in the same folder in TIFF format and labelled as Mask. The specific labelling was done to be traceable by the code as well as to be able to be used with any two components at any time.

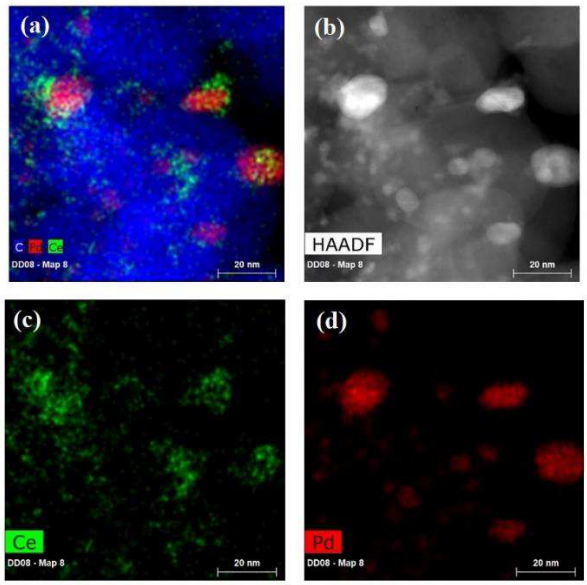


Figure 3: (a) Raw STEM/EDS elemental map of C, Ce & Pd (b) HAADF image (c) Raw Ce elemental map (d) Raw Pd elemental map

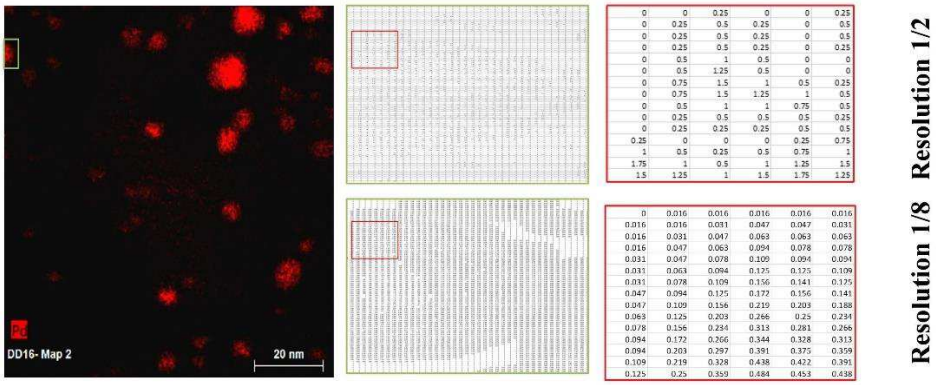


Figure 4: An example of magnified net count data from same region of same EDS map at two different processed map resolutions i.e., 1/2 and 1/8

Adjustment of Input Parameters

The text files of the required components were selected using the main window of the data processing interface as shown in Figure 5. The window allows user to change different parameters including pixel value (from raw images/maps), threshold value (to remove the noise), bin size and number of bins (for the area size histogram display) and type of output that is required (image, labels, histogram). The pixel size needs to be adjusted according to the pixel size of the raw map while appropriate threshold value needs to be selected to ensure that the code considers only the specified component's true signal and disregards any noise the map might contain. Appropriate bin size and number of bins needs to be selected for an appropriate representation of area (agglomerate, particle, etc.) size distribution histograms. The code automatically takes into account all the text files and mask image contained in a specific folder. Once the text file is selected and loaded, the

analysis is allowed to run. The input parameters selected to carry out the analysis of all the samples are given in Table 1.

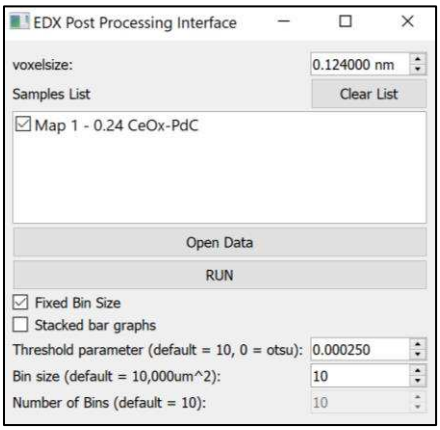


Figure 5: Overview of the EDS Post Processing Interface

| Image Magnification | Map Resolution | Map Filter | Image Filter | Pixel size | Threshold values (T) | Bin size |
|---|---|---|---|---|---|---|
| 910kx | 0.5 | Automatic | None | 0.124 nm | T = 0.00025 & T = 0.50 | 10 |

Table 1: Input Parameters

Post Processing Analysis

Once the parameters are set and the EDS Post Processing Program is allowed to run, the code runs the text files and scans through all the numeric values listed in the text file of each component and runs the thresholding algorithm. The Otsu and watershed algorithms (32,33) are used to threshold and segment both Pd and Ce maps, producing binarized masks. The mask is a binary image which has assigned zero (black color) to all pixels below the threshold value and 255 (white color) to all pixels above the threshold value. The code also eliminates the noise according to the user-defined threshold value and produces the final individual thresholded images. The program creates histograms for agglomerate size distribution of each component individually and collectively. It calculates the individual area occupied by each component, their overlap area, overlap percentage and the number and size of agglomerates. This information is automatically saved in an excel file at the completion of the analysis in the same directory. By default, all the measurements are carried out in unit of micrometer. For each map, two different net count threshold values (T) were selected i.e., T = 0.00025 and T = 0.5. These values were selected keeping in view the range of numerical values in input text files. The threshold value of 0.00025 is the lowest possible value no matter which map resolution is selected and therefore, includes all net intensity signals from a map (refer to Figure 5). However, there is at least one value lesser than 0.5 i.e., 0.25 in the text file for maps processed at resolution of 0.5 (input resolution), therefore it was chosen to selectively eliminate some of background signals or noise (having net count value of 0.25) from the thresholded image.

## Results and Discussion

As mentioned above, data processing method introduced in this study generates mainly two different forms of outputs: graphical and numerical. The different results that were obtained for each concentration of the catalyst samples under observation are therefore presented using these outputs. It can be aptly implied that the variety of outputs generated by the developed program in the form of masks, thresholded images, agglomerate size distribution charts, component area overlap, and calculation datasheet offers a wide range of result dataset which can be crucial for comprehensive study of any sample under consideration. Such comprehensive approach in data analysis, obtained by one imaging/spectroscopy method and data post-processing has not been reported for electrochemical systems, as per the authors' knowledge.

To evaluate the use of the discussed automatic EDS analysis interface, we investigated the effect of several parameters which are set before feeding the input data to the program. These parameters are associated with EDS map processing software Esprit and some of these parameters greatly influence the output given by the developed interface and might contribute to errors. The effect of a few of such parameters is discussed below:

### Effect of Different Parameters

Map Resolution. The effect of different map processing resolutions upon the graphical and numerical results is significant, an example of which is shown in Figure 6. There are four options for map resolutions in Esprit to choose from depending upon the pixel quality and processing time. The highest resolution is 1 and the lowest is 0.125. The lowest threshold value of 0.00025 was chosen to ensure inclusion of all signals from all the maps processed at different resolutions. The code did not work out the calculations for map resolution of 1 accurately and in most cases, it did not work at all with maps containing low intensity signals possibly because the developed program is not sensitive to the finer quality signals, and it eliminates many real signals along with noise. On contrary, the lowest map resolution blurred the real signals causing confusion between agglomerates and individual particles which contributed towards greater overlap values and incorporated plenty of noise thereby confirming that it is also not a good selection to begin with. Therefore, it was deduced that a reasonable selection to carry out the main calculations without compromising on the pixel quality was map resolution of 0.5. It must be noted here that the user must be extra cautious while choosing the threshold value when dealing with lower resolution maps since the low quality of image is prone to inclusion of more noise.

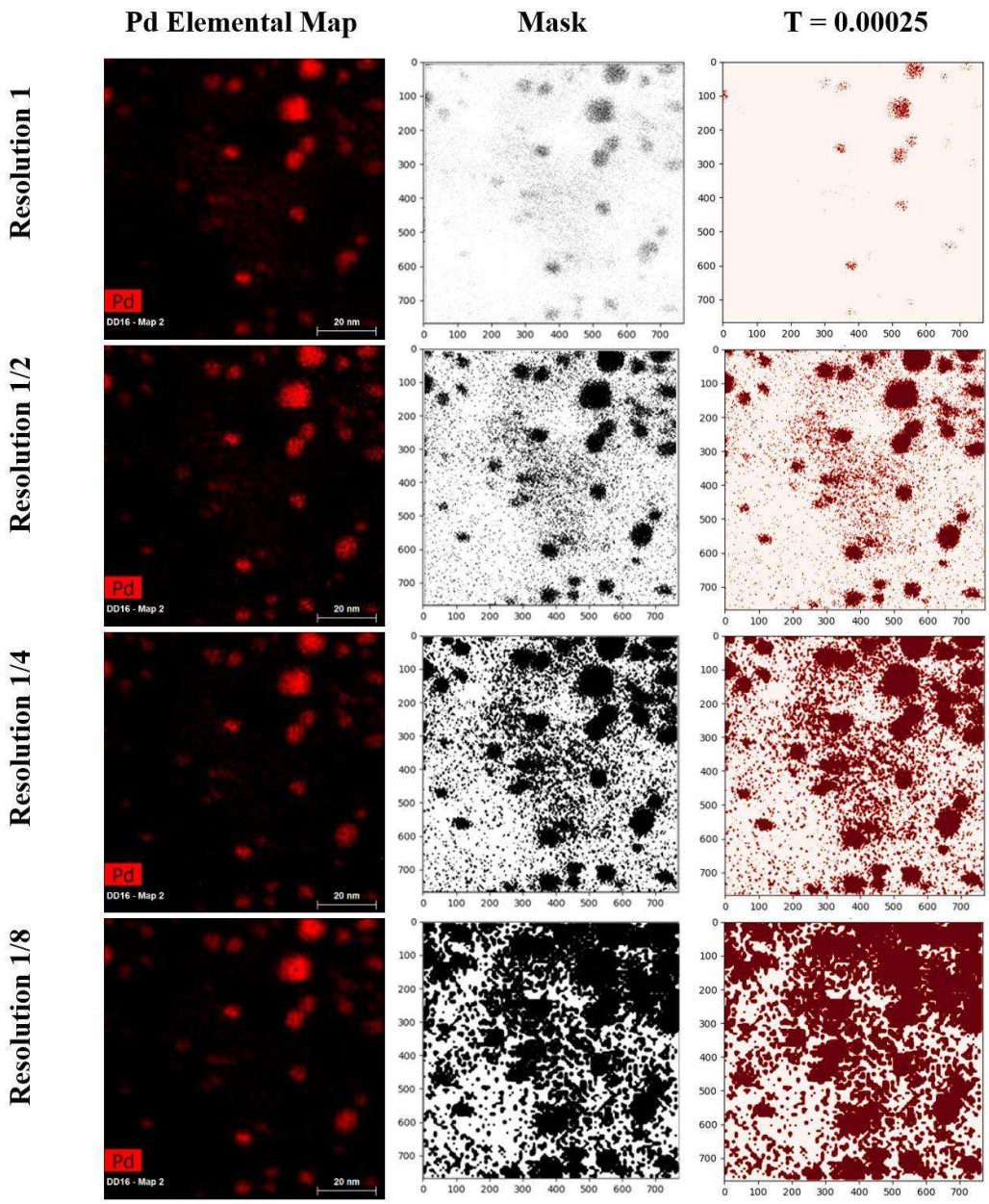


| T = 0.00025 | Resolution 1 | Resolution 1/2 | Resolution 1/4 | Resolution 1/8 |
|---|---|---|---|---|
| Pd Area ($nm^2$) | 82.62 | 1759.71 | 3637.27 | 5561.90 |

Figure 6: Effect of different map resolutions upon graphical and numerical results

Map and Image Filters. Esprit also allows users to choose a map and image filter out of different options. Map filter is applied directly on the net count signals contained in the map while image filter is applied only to the overlay image to enhance visibility of features. The name and effect of different map and image filters is demonstrated in Figure 7 and Figure 8, respectively. It can be clearly deduced from the Figure 7 that the effect of smooth and average map filter is quite comparable with same calculated results. However, the results for the automatic map filter are different and can be considered the best choice among the rest because it is based on local noise removal instead of uniform noise removal as in case of smooth and average filter.

However, it is very noticeable from Figure 8 that the different image filters have either no effect upon the results or the difference is too minimal to cause any change in the results. Since the effect of image filters is not as pronounced as the effect of map resolution and map filters, therefore, to carry out the analysis, the image filter was set to None.

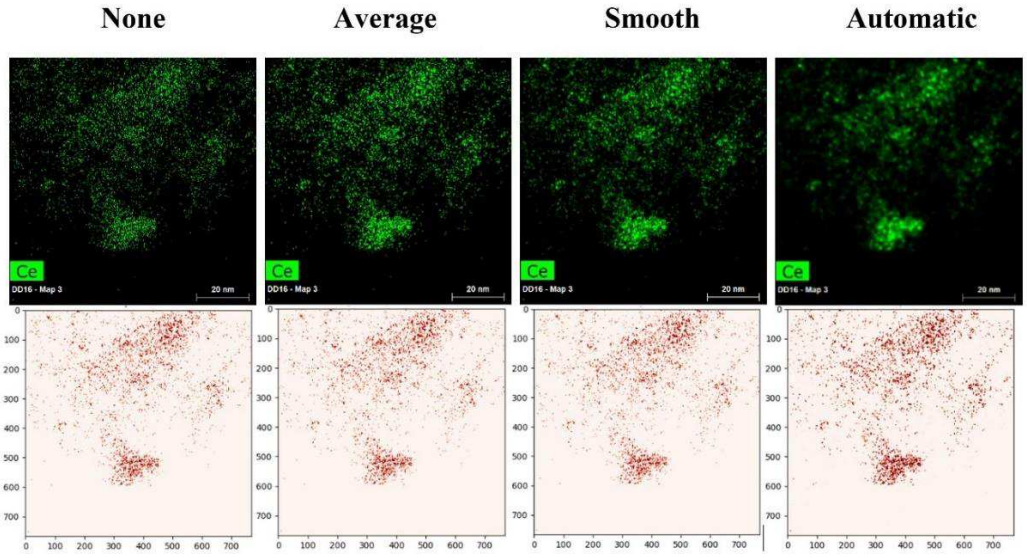


| T = 0.00025 | None | Average | Smooth | Automatic |
|---|---|---|---|---|
| Ce Area ($nm^2$) | 296.77 | 296.77 | 296.77 | 404.40 |

Figure 7: Effect of different map filters upon graphical and numerical results

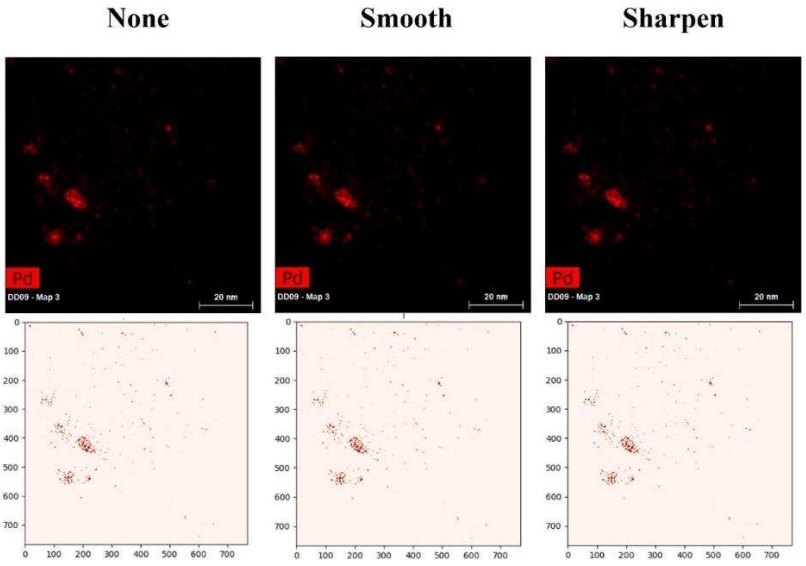


| T = 0.00025 | None | Smooth | Sharpen |
|---|---|---|---|
| Pd Area ($nm^2$) | 42.24 | 42.24 | 42.24 |

Figure 8: Effect of different image filters upon graphical and numerical results

Threshold value. The thresholding methods reported in the literature mostly rely upon the Otsu thresholding for image processing of greyscale values, which despite having many advantages, face certain limitations especially when dealing with images having large variance discrepancy and low contrast (34–37). Moreover, using greyscale images often complicates component differentiation, as one relies on greyscale contrast to differentiate between the components. To avoid such issues in this work, the differentiation between components (elements) is completed based on the spectral data, where spectral distribution maps of each element can be separately processed and thresholded. The introduced method uses a two-step noise removal, i.e., Otsu and a user-selected thresholding value for a finer noise removal. The user-selected thresholding value should be selected based on the lowest EDS spectra X-ray net count signal that is determined by Esprit software algorithm to be the background noise.

Three maps of each sample were run through the code using two different threshold values (T) i.e., 0.00025 and 0.50 and all the other input parameters were set to the same values as mentioned in Table 1 to investigate effect of thresholding upon the results. For the processed map resolution of 0.5, the lowest value in the net count data was found to be 0.25 indicating that anything lower than this value such as 0.00025 automatically includes all the net count signals within a map. It was also observed that no other net count value exists between 0.25 and 0.5 implying that the threshold value of 0.5 only excludes the minimum value signals of 0.25 and keep account of the rest. The resulting visual outputs of one map of each sample in the form of combined and individual elemental maps, masks and thresholded images and agglomerate size distribution charts are shown in Figure 9, 10 and 11, respectively.

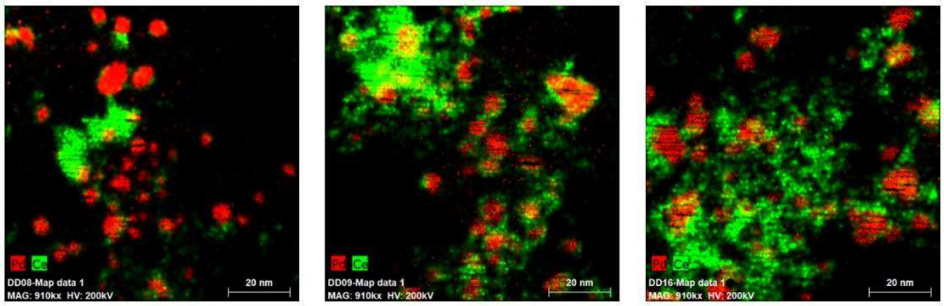


Figure 9: Processed elemental maps with map resolution of 1/2 showing overlap of Ce and Pd for sample (a) DD08 (b) DD09 (c) DD16

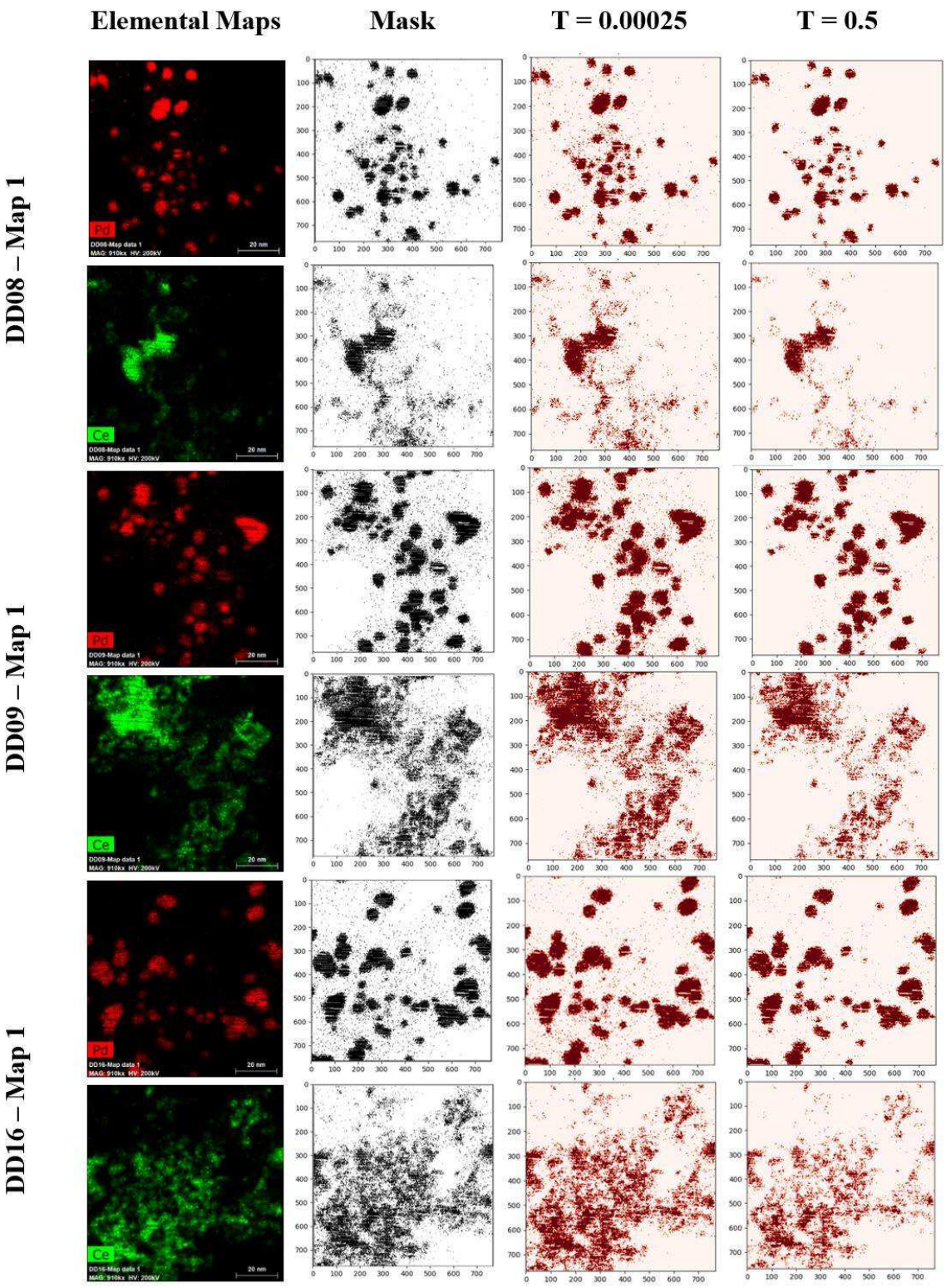


Figure 10: Elemental maps of Ce and Pd and corresponding mask and thresholded images with threshold values: T = 0.00025 and T = 0.5

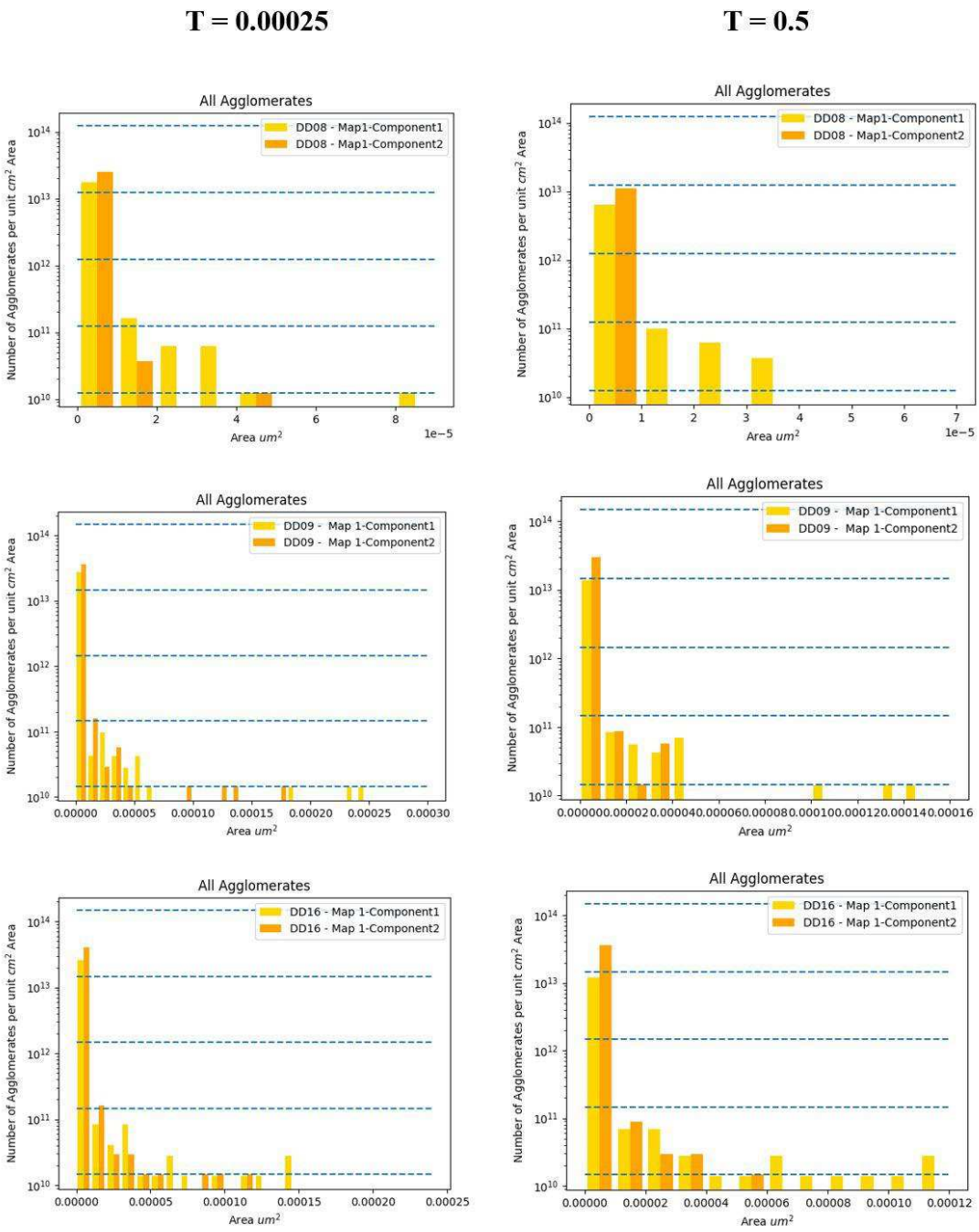


Figure 11: Agglomerate size distribution charts for T = 0.00025 and T = 0.5 map of each sample in Figure 9

All the calculations carried out by the code for the specified threshold values are compiled in Table 2. A graphical representation of average percentage of Pd in contact with Ce (Pd-Ce overlap) for each threshold value and each sample is shown in Figure 12. The analysis of the component overlap presented here is, in the authors' opinion, a novel approach, which has not been reported in the previous literature (38–41).

| Samples (T = 0.00025) | Average Pd Area ($nm^2$) | Average Ce Area ($nm^2$) | Average Overlap Area ($nm^2$) |
|---|---|---|---|
| DD08 | 626 | 576 | 164 |
| DD09 | 655 | 736 | 370 |
| DD16 | 1639 | 2266 | 652 |

| Samples (T = 0.5) | Average Pd Area ($nm^2$) | Average Ce Area ($nm^2$) | Average Overlap Area ($nm^2$) |
|---|---|---|---|
| DD08 | 410 | 279 | 55 |
| DD09 | 481 | 431 | 194 |
| DD16 | 1155 | 1528 | 258 |

Table 2: Computed results for threshold value T = 0.00025 and T = 0.5

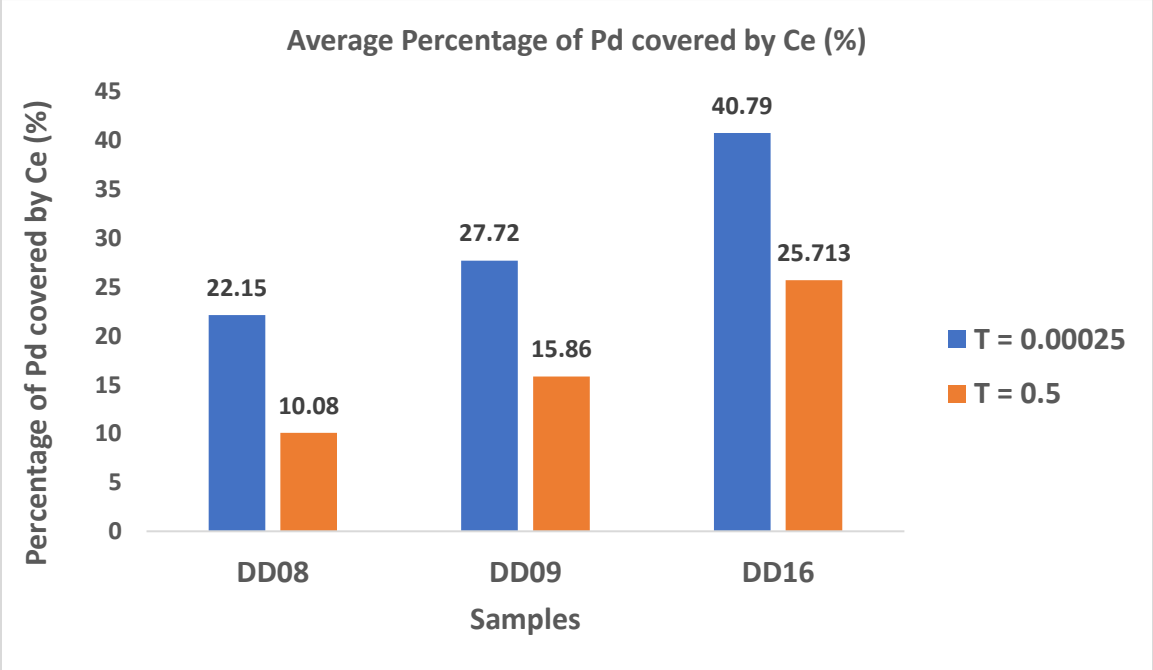


Figure 12: Results for average percentage of Pd covered by Ce by each sample with threshold value of T = 0.00025 and T = 0.5

As evident from the results, sample DD16 shows the highest average Pd area among the rest which also signifies that sample DD16 has relatively larger Pd particles as compared to the other samples. Furthermore, as expected, with increasing concentration of Ce, a considerable increase in Pd area percentage in contact with $CeO_x$ (overlap percentage) can be observed. It can also be inferred that the thresholding value has a very pronounced effect upon all the calculations showing a decrease of about 40-54% in the overlap percentage with the increase in thresholding value from 0.00025 to 0.5. Besides, comparing specific regions of original maps with the thresholded maps and their EDS spectra also represents that maps thresholded with 0.00025 show more signs of inclusion of noise but the maps

thresholded with 0.5 are relatively cleaner and hence can be used to acquire more accurate results.

Generally, most studies involving data processing have computed and reported results based upon the imaging data alone (42–47). On contrary, extraction of microstructural information from STEM in combination with elemental map data from EDS is what gives this method its distinctiveness. Furthermore, automatic computation of agglomerate size distribution and overlap area of the particles has not been reported before, further promoting exclusivity of the developed method.

## Conclusion

The data processing framework introduced in this study is a unique, automated, and promising method for an automatic post processing of STEM-EDS data. The code runs pixel by pixel numerical analysis keeping into account distinct particles in the maps which might be overlooked during manual analysis, thus, it can effectively resolve problems associated with extensive and exhaustive analysis of larger data sets. However, it can be concluded that the calculations also depend heavily upon the EDS map processing software used to extract data for the code. The study also points out that the selection of an appropriate threshold value is vital to ensure good precision of results generated by the program. Minor improvements such as automatic selection of local threshold values and optimizing the code to work with more than two components at the same time can help extend the serviceability of the developed script. Furthermore, the code can be tailored to detect and analyze other microstructural features and can be optimized to be used with other formats of materials characterization data. Experimentally derived electrochemical performance data of the samples investigated in this study can be used to verify the accuracy of the developed method. Such information can be of paramount importance to research focusing on improving the efficiency of Pd-$CeO_x$ based catalysts for AEMFCs by relating the overlap area to the electrochemical performance.

## Acknowledgements

We are immensely grateful to the U.S. Fulbright Foreign Scholarship program for providing the opportunity and funding to carry out this research work.

## References

1. Duval L, Moreaud M, Couprie C, Jeulin D, Talbot H, Angulo J. Image processing for materials characterization: Issues, challenges and opportunities. 2014 IEEE Int Conf Image Process ICIP 2014. 2014;4862–6.
2. Xia D, Song S, Tao L, Qin Z, Wu Z, Gao Z. Journal of Materials Science & Technology Review-material degradation assessed by digital image processing : Fundamentals , progresses , and challenges. J Mater Sci Technol [Internet]. 2020;53:146–62. Available from: https://doi.org/10.1016/j.jmst.2020.04.033
3. Hou Y, Li Q, Zhang C, Lu G, Ye Z, Chen Y, et al. The State-of-the-Art Review on Applications of Intrusive Sensing, Image Processing Techniques, and Machine Learning Methods in Pavement Monitoring and Analysis. Engineering [Internet].

2021;7(6):845–56. Available from: https://doi.org/10.1016/j.eng.2020.07.030
4. Bae SM, Jung HY, Lee JH, Hwang JH. Microstructural characterization of composite electrode materials in solid oxide fuel cells via image processing analysis. J Korean Ceram Soc. 2010;47(1):86–91.
5. Jankovic J, Zhang S, Putz A, Saha MS, Susac D. Multiscale imaging and transport modeling for fuel cell electrodes. J Mater Res. 2019;34(4):579–91.
6. Sabharwal M, Putz AMV, Susac D, Jankovic J, Secanell M. Improving FIB-SEM Reconstructions by Using Epoxy Resin Embedding. ECS Trans. 2017;77(11):1337–49.
7. Sabharwal M, Pant LM, Putz A, Susac D, Jankovic J, Secanell M. Analysis of Catalyst Layer Microstructures: From Imaging to Performance. Fuel Cells. 2016;16(6):734–53.
8. Kumar Boyat A, Kumar Joshi B. Signal & Image Processing. An Int J. 2015;6(2).
9. Patidar P, Gupta M, Srivastava S, Nagawat AK. Image De-noising by Various Filters for Different Noise. Int J Comput Appl. 2010;9(4):45–50.
10. Campbell A, Murray P, Yakushina E, Marshall S, Ion W. New methods for automatic quanti fi cation of microstructural features using digital image processing. Mater Des [Internet]. 2018;141:395–406. Available from: https://doi.org/10.1016/j.matdes.2017.12.049
11. Biswal SR, Sahoo T, Sahoo S. Prediction of grain boundary of a composite microstructure using digital image processing: A comparative study. Mater Today Proc [Internet]. 2021;41:357–62. Available from: https://doi.org/10.1016/j.matpr.2020.09.559
12. Soosai MR, Joshya YC, Kumar RS, Moorthy IG, Karthikumar S, Chi NTL, et al. Versatile image processing technique for fuel science: A review. Sci Total Environ [Internet]. 2021;780:146469. Available from: https://doi.org/10.1016/j.scitotenv.2021.146469
13. Chen Z, Wu X. Research on regional energy efficiency based on GIS technology and image quality processing. J Vis Commun Image Represent [Internet]. 2019;62:410–7. Available from: https://doi.org/10.1016/j.jvcir.2019.06.008
14. Cai W, Wen X, Wang S, Wang L. A real-time detection method of building energy efficiency based on image processing. J Vis Commun Image Represent [Internet]. 2019;60:295–304. Available from: https://doi.org/10.1016/j.jvcir.2019.02.032
15. Salamanca S, Merchán P, Adán A, Pérez E. An appraisal of the geometry and energy efficiency of parabolic trough collectors with laser scanners and image processing. Renew Energy. 2019;134:64–77.
16. Shin HS, Kwon OJ, Oh BS. Correlation between performance of polymer electrolyte membrane fuel cell and degradation of the carbon support in the membrane electrode assembly using image processing method. Int J Hydrogen Energy [Internet]. 2018;43(45):20921–30. Available from: https://doi.org/10.1016/j.ijhydene.2018.09.016
17. Klingele M, Zengerle R, Thiele S. Quantification of artifacts in scanning electron microscopy tomography: Improving the reliability of calculated transport parameters in energy applications such as fuel cell and battery electrodes. J Power Sources [Internet]. 2015;275:852–9. Available from: http://dx.doi.org/10.1016/j.jpowsour.2014.11.053
18. Cetinbas FC, Ahluwalia RK, Kariuki N, De Andrade V, Fongalland D, Smith L, et al. Hybrid approach combining multiple characterization techniques and simulations for microstructural analysis of proton exchange membrane fuel cell

electrodes. J Power Sources [Internet]. 2017;344:62–73. Available from: http://dx.doi.org/10.1016/j.jpowsour.2017.01.104
19. Muto H, Shimada A, Kaneko T, Erdman N, Nielsen C. SEM-EDS Automated Particles Analysis— " INCA Mineral " — Mineral Compositions of Koujaku Granite and Hakkoda Pyroclastic Flow Deposition. J Geol Soc Japan Earth Sci (Chikyu Kagaku) J Geogr. 1972;78(1):2–3.
20. Anderhalt R, Swenson L. Applications for Automated Particle Analysis. Micros Today. 2006;14(5):22–7.
21. Lang C, Hiscock M. Automated Analysis of EDS Maps. Microsc Microanal. 2016;22(S3):122–3.
22. Information P. ZEISS SmartPI Your Automated SEM Particle Analysis and Classification Solution Detect , Analyze and Classify Particles. :1–19.
23. Note A. ZEISS SmartPI Automated Identification of Asbestos ZEISS SmartPI Automated Identification of Asbestos.
24. Scimeca M, Bischetti S, Bonanno E. Energy Dispersive X-ray (EDX) Microanalysis in Biomedical Research. Lett Heal Biol Sci. 2016;1(1):10–1.
25. Jany BR, Janas A, Krok F. Automatic microscopic image analysis by moving window local Fourier Transform and Machine Learning. Micron [Internet]. 2020;130(July 2019):102800. Available from: https://doi.org/10.1016/j.micron.2019.102800
26. Biswas S. Automated Asbestos Analysis using Semantic Segmentation. 2020;(March).
27. Zhang J, Zhu W, Huang T, Zheng C, Pei Y, Shen G, et al. Recent Insights on Catalyst Layers for Anion Exchange Membrane Fuel Cells. Adv Sci. 2021;2100284:1–26.
28. Cao Y, Ran R, Wu X, Zhao B, Wan J, Weng D. Comparative study of ageing condition effects on Pd/Ce0.5Zr 0.5O2 and Pd/Al2O3 catalysts: Catalytic activity, palladium nanoparticle structure and Pd-support interaction. Appl Catal A Gen. 2013;457:52–61.
29. Kolli T, Rahkamaa-Tolonen K, Lassi U, Savimäki A, Keiski RL. Comparison of catalytic activity and selectivity of Pd/(OSC + Al 2O3) and (Pd + OSC)/Al2O3 catalysts. Catal Today. 2005;100(3–4):297–302.
30. Darija S et al. Towards Understanding of the Anode Catalyst Layer Structure for Extended Reversal Tolerance: An Advanced Characterization Approach. ECS Meet Abstr [Internet]. 2016;MA2016-02(2593). Available from: http://dx.doi.org/10.1149/MA2016-02/38/2593
31. Singh RK, Davydova ES, Douglin J, Godoy AO, Tan H, Bellini M, et al. Synthesis of CeOx-Decorated Pd/C Catalysts by Controlled Surface Reactions for Hydrogen Oxidation in Anion Exchange Membrane Fuel Cells. Adv Funct Mater. 2020;30(38).
32. Hoang ND. Detection of Surface Crack in Building Structures Using Image Processing Technique with an Improved Otsu Method for Image Thresholding. Adv Civ Eng. 2018;2018.
33. Salman N. Image Segmentation Based on Watershed and Edge Detection Techniques. Int Arab J Inf Technol. 2006;3(2):104–10.
34. Stuckner J, Frei K, McCue I, Demkowicz MJ, Murayama M. AQUAMI: An open source Python package and GUI for the automatic quantitative analysis of morphologically complex multiphase materials. Comput Mater Sci [Internet]. 2017;139:320–9. Available from:

http://dx.doi.org/10.1016/j.commatsci.2017.08.012
35. Bourrous S, Ribeyre Q, Lintis L, Yon J, Bau S, Thomas D, et al. A semi-automatic analysis tool for the determination of primary particle size, overlap coefficient and specific surface area of nanoparticles aggregates. J Aerosol Sci [Internet]. 2018;126(September):122–32. Available from: https://doi.org/10.1016/j.jaerosci.2018.09.001
36. Filho PPR, Da Silveira Cavalcante T, De Albuquerque VHC, Tavares JMRS. Brinell and Vickers hardness measurement using image processing and analysis techniques. J Test Eval. 2010;38(1).
37. Garrido I, Lagüela S, Sfarra S, Madruga FJ, Arias P. Automatic detection of moistures in different construction materials from thermographic images. J Therm Anal Calorim. 2019;138(2):1649–68.
38. White RT, Wu A, Najm M, Orfino FP, Dutta M, Kjeang E. 4D in situ visualization of electrode morphology changes during accelerated degradation in fuel cells by X-ray computed tomography. J Power Sources. 2017;350:94–102.
39. Xu H, Bührer M, Marone F, Schmidt TJ, Büchi FN, Eller J. Optimal Image Denoising for In Situ X-ray Tomographic Microscopy of Liquid Water in Gas Diffusion Layers of Polymer Electrolyte Fuel Cells. J Electrochem Soc. 2020;167(10):104505.
40. Satija R, Jacobson DL, Arif M, Werner SA. In situ neutron imaging technique for evaluation of water management systems in operating PEM fuel cells. J Power Sources. 2004;129(2):238–45.
41. Kneer A, Jankovic J, Susac D, Putz A, Wagner N, Sabharwal M, et al. Correlation of Changes in Electrochemical and Structural Parameters due to Voltage Cycling Induced Degradation in PEM Fuel Cells. J Electrochem Soc. 2018;165(6):F3241–50.
42. Codaro EN, Nakazato RZ, Horovistiz AL, Ribeiro LMF, Ribeiro RB, Hein LRO. An image processing method for morphology characterization and pitting corrosion evaluation. Mater Sci Eng A. 2002;334(1–2):298–306.
43. Bescond A, Yon J, Ouf FX, Ferry D, Delhaye D, Gaffié D, et al. Automated determination of aggregate primary particle size distribution by tem image analysis: Application to soot. Aerosol Sci Technol. 2014;48(8):831–41.
44. Bessa IS, Castelo Branco VTF, Soares JB. Evaluation of different digital image processing software for aggregates and hot mix asphalt characterizations. Constr Build Mater [Internet]. 2012;37:370–8. Available from: http://dx.doi.org/10.1016/j.conbuildmat.2012.07.051
45. Scozzafava A, Tomesani L, Zucchelli A. Image analysis automation of spheroidal cast iron. J Mater Process Technol. 2004;153–154(1–3):853–9.
46. Sochan A, Zieliński P, Bieganowski A. Selection of shape parameters that differentiate sand grains, based on the automatic analysis of two-dimensional images. Sediment Geol. 2015;327:14–20.
47. Liu C, Shi B, Zhou J, Tang C. Quantification and characterization of microporosity by image processing, geometric measurement and statistical methods: Application on SEM images of clay materials. Appl Clay Sci [Internet]. 2011;54(1):97–106. Available from: http://dx.doi.org/10.1016/j.clay.2011.07.022